Experimental Monitoring of Nonlinear Wave Interactions Under Uniaxial Load

Alison Malcolm[1], Lauren Hayes[2], Kamal Moravej[1], Andrey Melnikov[1], Kristin Poduska[1], and Stephen Butt[1]

[1]Memorial University of Newfoundland
[2]Memorial University of Newfoundland, now at Innovation and Scientific Development Canada

November 23, 2022

Abstract

It is now well-established that earthquakes change the seismic velocity of the near surface. There is certainly some understanding of what mechanisms are responsible for these changes, but there remain many questions. One of these open questions is how cracks and other microstructures within the rock control these changing velocities. Here we look at the nonlinear interaction of two waves, one of which (the PUMP) simulates the effect of an earthquake and the other (the probe) senses the changes in the travel time caused by the passage of the PUMP wave. We use a sandstone sample that is established to have a nonlinear response that depends on the orientation of the sample layering. We study two samples with different orientations of this layering, which we infer to be different orientations of the micro-structure. We show that the dependence of these changes on applied load are exponential, with a characteristic load of 11.4-12.5~MPa that is independent of sample orientation and probe wavetype (P or S); this value agrees with results from the literature.

Experimental Monitoring of Nonlinear Wave Interactions Under Uniaxial Load

Alison Malcolm [1], **Lauren Hayes**[1], **Kamal Moravej**[1], **Andrey Melnikov**[1], **Kristin M. Poduska**[3], **Stephen Butt**[2]

[1]Department of Earth Sciences, Memorial University of Newfoundland

[2]Department of Engineering, Memorial University of Newfoundland

[3]Department of Physics and Physical Oceanography, Memorial University of Newfoundland

Key Points:

- We present a simple experimental configuration for measuring changes in the nonlinear response of rocks under uniaxial load.
- We fit measured changes in the nonlinear response to a simple model that illustrates a characteristic load.
- Our data indicate that nonlinear measurements are more sensitive to changes in aligned structures (e.g. cracks/layers) than are velocities.

Corresponding author: Alison Malcolm, `amalcolm@mun.ca`

Abstract

It is now well-established that earthquakes change the seismic velocity of the near surface. There is certainly some understanding of what mechanisms are responsible for these changes, but there remain many questions. One of these open questions is how cracks and other microstructures within the rock control these changing velocities. Here we look at the nonlinear interaction of two waves, one of which (the PUMP) simulates the effect of an earthquake and the other (the probe) senses the changes in the travel time caused by the passage of the PUMP wave. We use a sandstone sample that is established to have a nonlinear response that depends on the orientation of the sample layering. We study two samples with different orientations of this layering, which we infer to be different orientations of the micro-structure. We show that the dependence of these changes on applied load are exponential, with a characteristic load of 11.4-12.5 MPa that is independent of sample orientation and probe wavetype (P or S); this value agrees with results from the literature.

Plain Language Summary: After a large earthquake, it takes the materials surrounding the epicentre some time to return to their original form. This includes changes in the speed at which waves travel through the surrounding material. We do not fully understand why this happens or more specifically what happens to cause these changes in speed. To improve our understanding, we do experiments on rocks in the laboratory to try to isolate different characteristics of the material that may control these changes. Here we look at how changes in the applied load (how much force we apply to squeeze the rock) changes these signals. We find that there is a characteristic load that is independent of the orientation of the layering in the sample and they types of waves we use.

1 Introduction

Understanding the nonlinearity in the Earth's response to waves is becoming more important as we try to understand why and how large earthquakes change the properties of the Earth and to understand reservoirs in more detail. For the former, many studies show that the Earth's seismic velocity drops, and subsequently recovers, as a result of the passage of large waves from an earthquake (see Wang et al. (2019) for a good introduction and Aoki (2015) for a concise overview of recent observations and the the-

ory behind nonlinear elasticity). At a smaller scale, both induced and pre-existing fractures represent pathways for fluids in reservoirs (e.g. CO_2, water, oil and gas). A nonlinear Hooke's law is becoming a recognized driver of change in such reservoirs (Asaka et al., 2018). Here, we attempt to simulate this response using a PUMP/probe experiment (Renaud et al., 2008, 2011; Gallot et al., 2015) that tracks the response of a low-amplitude probe wave as forced by a large-amplitude PUMP wave. (The terminology 'PUMP' for the stronger wave and 'probe' for the weaker sensing wave is well-established. For clarity, we use uppercase 'PUMP' to indicate the stronger wave.) We use a uniaxial load to change the properties of existing fractures to learn how these properties affect the nonlinear signal.

The first reports of non-linear behaviors in rocks (Birch, 1960) and other materials (Hughes & Kelly, 1953) are decades old. Many theoretical models address this nonlinearity, ranging from classical nonlinearity (involving higher-order expansions of Hooke's Law) to various phenomenological models to describe additional effects observed in rocks that are not predicted by the classical theory. A detailed overview of this theory is beyond the scope of this experimental paper, but we summarize relevant literature here. Norris and Johnson (1997) derive the equations of motion for classical nonlinearity. Sens-Schönfelder et al. (2018) give a thorough overview of recent classical and non-classical nonlinear theory; Ostrovsky and Johnson (2001) summarize earlier studies. Work relating to cracks is surveyed by Broda et al. (2014). Scalerandi et al. (2018) give an excellent overview of non-destructive testing applications, especially the influence of cracks and micro-structures on the nonlinear response. Guyer and Johnson (2009) give a more detailed treatment of both classical and non-classical theories.

We use classical PUMP/probe experiments that in some sense go back to at least Hughes and Kelly (1953) who study changes in a probe wave caused by static deformations (their PUMP). The most common variant in the current literature is Dynamic Acousto-Elastic Testing method (DAET, Renaud et al. (2008, 2012)). In DAET, a resonant mode is excited in the sample (the PUMP) and that mode is then analyzed with a high-frequency probe wave. Rivière et al. (2013) give a careful overview of both the experimental setup and data processing to help understand and analyze DAET data; Rivière et al. (2015) give a detailed comparison of DAET to the more classical Nonlinear Resonance Ultrasound Spectroscopy (NRUS). Remillieux et al. (2017) provide a large NRUS dataset, which stimulated model development to better understand the data (Lott, Payan, et al., 2016;

Lott, Remillieux, et al., 2016; Lott et al., 2017). Sens-Schönfelder and Eulenfeld (2019) use Earth tides as a PUMP and noise as probe in a field experiment analogous to DAET. Muir et al. (2020) use a hammer source in a similar setup to ours designed for much larger samples. Gallot et al. (2015) develop a method that relies on transient waves, which we use in this work. Modeling for this particular experiment is a challenge because the sample experiences two dynamic forces (PUMP, probe) and one static force (press). Gallot et al. (2015); Rusmanugroho et al. (2020) describe a relatively simple model that is most appropriate to our specific experiments.

We focus on aligned cracks and their response to applied loads. Aligned cracks are common in the Earth, wherein tectonic forces can guide crack formation, opening and closing; in-situ rocks are also generally under load (Alkhalifah & Tsvankin, 1995). It remains difficult to definitively separate the response of cracks from other signals, like heterogeneity and intrinsic anisotropy, at second-order (standard linear elasticity) and at higher orders. TenCate et al. (2016) give a first attempt at characterizing the importance of microstructure orientation relative to nonlinear wave interactions. A numerical model of these results, given in Rusmanugroho et al. (2020), suggests that what TenCate et al. (2016) interpret as a set of aligned cracks is likely more complicated, with evidence that nonlinear response should vanish when crack normals are perpendicular to a P-wave probe particle motion.

Here, we aim to separate these signals by running nonlinear elastic experiments repeatedly for a rock under different uniaxial loads. This follows from work by: Zinszner et al. (1997) on classical nonlinear resonance under a variety of loads and saturations, Rivière et al. (2016) who study DAET under a variety of pressures, and Simpson et al. (2021) who monitor velocity changes over a range of confining pressures. These earlier works suggest an exponential decrease in nonlinearity with increasing load, with a characteristic pressure $\sim$10 MPa (Rivière et al., 2016) for sandstones and 1 MPa (Simpson et al., 2021) for rocks from an active fault zone.

2 Methods

2.1 Sample Descriptions

We examine two samples of Crab Orchard Sandstone (COS) from Cumberland, Tennessee, which is beige, fine-grained, and cross-bedded with sub rounded grain shapes and

	L_x (mm)	L_y (mm)	L_z (mm)	ρ	V_{Px}	V_{Py}	V_{Sx}	V_{Sy}	γ_P	γ_S
Sample 1	126	155	52	2.4	3.2	3.05	2.24	2.22	5.1%	0.85%
Sample 2	125	154	52	2.5	3.27	3.23	2.25	2.19	1.1%	2.5%

Table 1. Physical parameters of our samples. The dimensions are measured with calipers and the velocities using the probe transducers by measuring the travel time of the P- and S-waves across the sample in all three dimensions, L_j is the length along the jth axis; V_{Mj} is the velocity of wave mode M (P or S) propagating in direction j; γ_M is the M-mode anisotropy.

no preferred grain alignment. It is compositionally and texturally mature (composition: 80% quartz, 10% orthoclase, 9% cement (clays and micas), 1% mica). This composition is similar to that of Benson et al. (2005) who conclude that the cement destroys much of the porosity, leaving porosity in the form of cracks and pores. TenCate et al. (2016) find that COS exhibits strong anisotropy in its nonlinear response. We report physical parameters of our samples in Table 1. Density is sample mass divided by volume; velocities are the travel distance divided by the travel time of the wave (recorded with probe transducers at the probe frequency). We compute anisotropy using

$$\gamma = \frac{V^{max} - V^{min}}{V^{ave}}$$

where V^{max} is the maximum of the velocities in the two recorded orientations, V^{min} is the minimum and V^{ave} is the average velocity. Both samples exhibit P- and S-wave anisotropy, although Sample 1 has much stronger P-wave anisotropy whereas Sample 2 has stronger S-wave anisotropy. See Supplementary Text S1 for more velocity measurement details.

2.2 Experimental Setup

We use the setup described in Gallot et al. (2015); TenCate et al. (2016) and place it inside a hydraulic press, (Figure 1). This design is similar to DAET, with the exception that our PUMP wave is a propagating S-wave, not a resonance mode. We monitor perturbations induced by a strong PUMP wave by using a weaker probe wave as a sensor. To ensure that the probe is indeed weak, we use a signal that is two orders-of-magnitude weaker in strain for the probe (order of magnitude of the strain is 10^{-8}) than for the PUMP (10^{-6}). Details of this strain measurement are given in Supplementary Text S3.
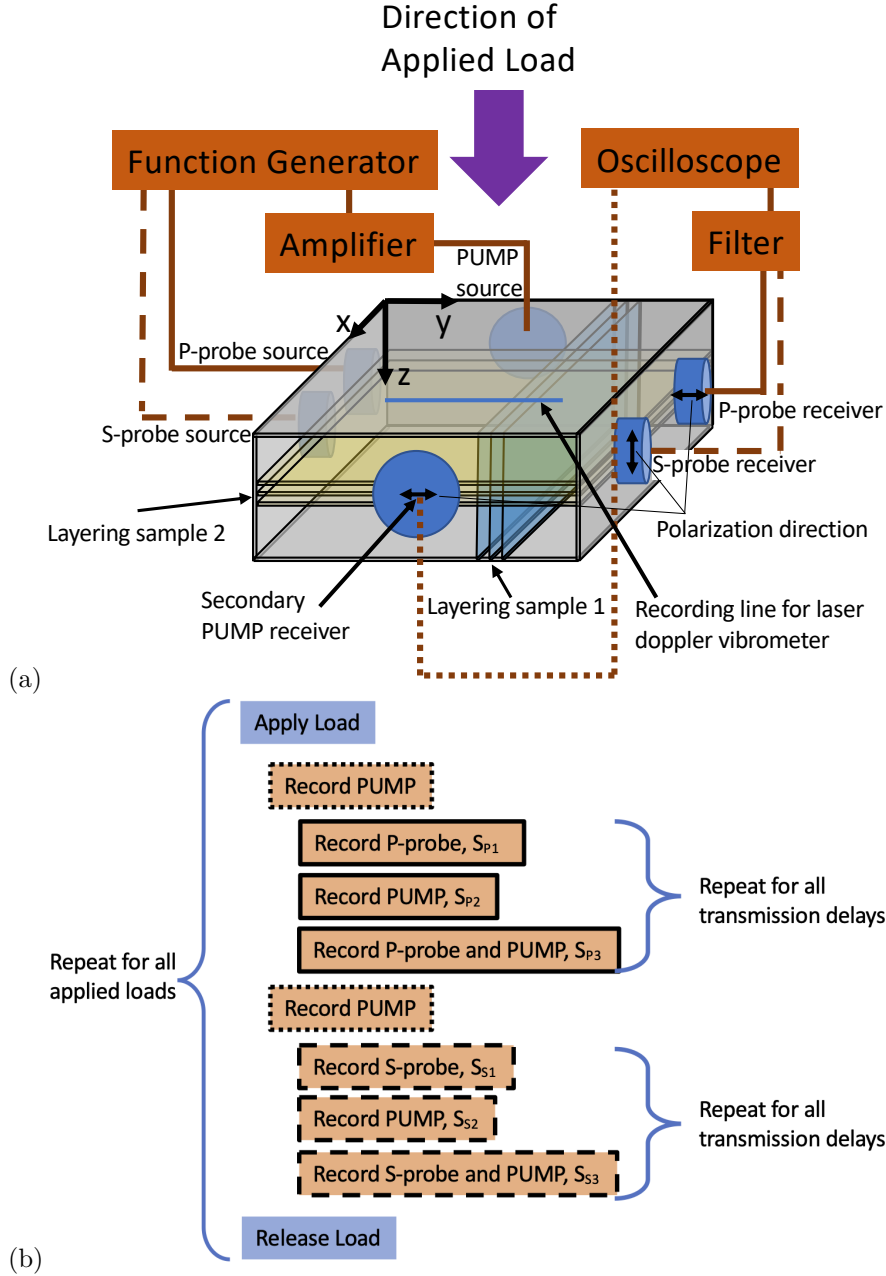
(a)

(b)

Figure 1. (a) The experimental setup, including the coordinate system to be used later. In all experiments the PUMP source is connected to the function generator and amplifier. Solid lines denote connections for P-probe experiments; dashed lines correspond to S-probe experiments; dotted lines correspond to PUMP recording only. The polarization directions are noted on each receiver (b) Summary of experimental protocols. The line style on the boxes (solid, dashed, or dotted) indicates the receiver setup, as described for (a).

wave	transducer resonance	driving freq.	cycles	polar. dir.	prop. dir.	amp	*approx* strain	λ
PUMP	100 kHz	90 kHz	4	y	x	10 V	10^{-6}	24 mm
P-probe	1 MHz	1 MHz	1	y	y	0.1 V	10^{-8}	3.6 mm
S-probe	1 MHz	1 MHz	1	z	y	0.1 V	10^{-8}	2.2 mm

Table 2. Summary of experimental parameters: prop. dir. = propagation direction, polar. dir. = polarization direction, λ = wavelength, and amp = amplitude (peak-to-peak voltage) of the input signal before going through the (50x) amplifier.

Figure 1 shows our experimental setup and Table 2 summarizes the experimental parameters. For all experiments, we use a 90 kHz S-wave PUMP signal propagating along the x-direction with polarization in the y-direction. We explore two different kinds of probes: a P-wave propagating and polarized along the y direction, and an S-wave probe propagating along the y direction with polarization in the z-direction. We note that past experiments by Gallot et al. (2015) find the largest signal when the particle motion of the PUMP and probe are aligned. Further experimental details, including rationales for frequency choices and travel time delay details, are discussed in Supplementary Text S1, and detailed parameter settings are given in Supplementary Text S2.

We sense the change in the probe travel time as the PUMP wave passes. To do this, we must measure the travel time delay in the probe as it interferes with different phases of the PUMP wave. We do this by controlling the transmission delay, which is the time between the emission of the PUMP and probe signals. In our experiments, this delay is controlled by the function generator, by syncing the triggering of the channel emitting the probe signal to the channel emitting the PUMP signal, adding a variable delay to the probe signal. This transmission delay will be the independent variable (x-axis) on the plots of our experimental results.

To measure the changing travel time, we record three signals on the positive y-face using transducers identical to those used to excite the probe (i.e. P-wave transducers for the P-wave probe and S-wave transducers for the S-wave probe). The three signals that we record (illustrated in Figure 2(b)) are:
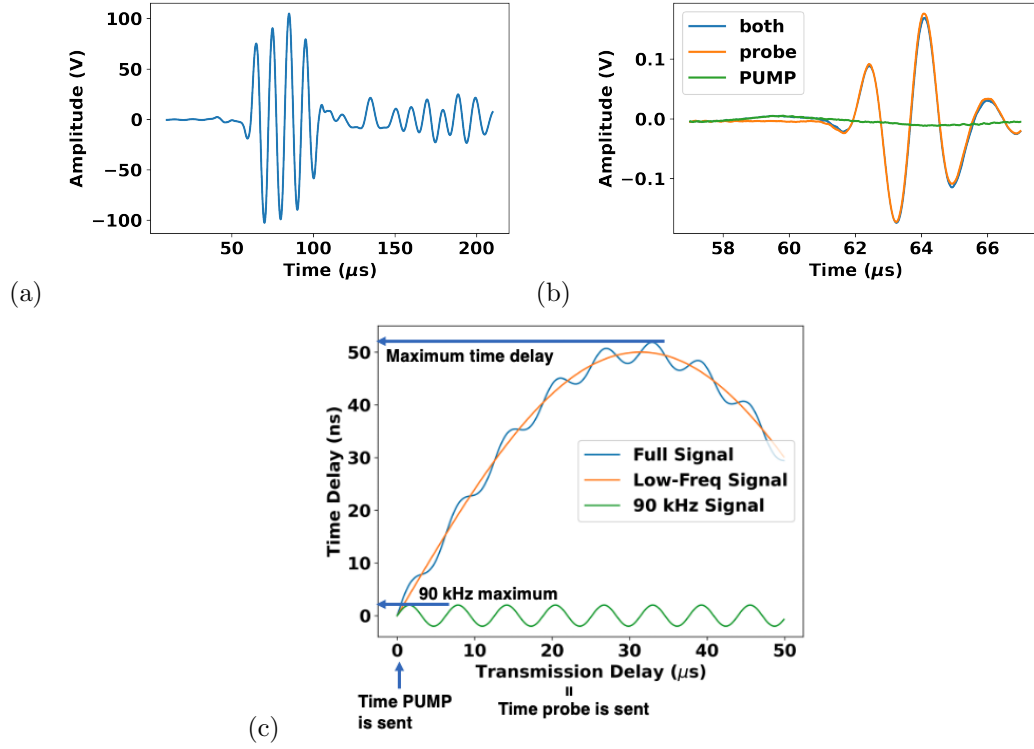
1. S_1 the probe alone,

(a)

(b)

(c)

Figure 2. (a) PUMP signal recorded on the x-face of the sample opposite the PUMP generating S-wave transducer. (This signal uses the recording setup with the dashed lines in Figure 1.) (b) Signals recorded to estimate travel time delays on the P-transducer on the y-face opposite the P-probe source transducer. (These signals use the recording setup shown with the solid lines in Figure 1.) The three signals shown are with the PUMP only (S_2), the probe only (S_1) and both together, (S_3). These signals have been filtered to remove as much of the PUMP signal as possible. Note the different scales in both time and amplitude. (c) Cartoon to illustrate the format of the data plots (shown in Figure 6).

2. S_2 the PUMP alone,

3. S_3 the PUMP and probe together.

As it is our goal to compare the probe signal present in S_3 to the unperturbed probe in S_1, we need to remove the PUMP from S_3. We do this in two parts. The first is the high-pass physical filter shown in Figure 1. This significantly reduces the amplitude of the PUMP signal, allowing us to record the probe signal with sufficiently high precision, but does not completely eliminate it. Because the filter is imperfect, we then form $S_4 = S_3 - S_2$ to remove the remaining PUMP signal and obtain an estimate of the perturbed probe signal. The travel time delay is the difference in the arrival time between the original probe (in S_1) and perturbed probe (in S_4). We measure this delay using cross-correlations, as explained by Catheline et al. (1999); we give further details on this in Supplementary Text S4. Having measured one travel time delay, we then change the transmission delay time between the PUMP and probe and measure the same three signals to obtain the next data point. This is summarized in Figure 1(b), and a cartoon of the resulting experimental data to illustrate the transmission delay is shown in Figure 2(c). The data collection takes approximately one hour for a single applied stress and PUMP/probe combination. For each sample and applied load we collect two datasets, one with a P-wave probe and the other with an S-wave probe. All data use an S-wave PUMP. Hayes and Malcolm (2017) find that the relative polarizations of the two S-waves have a small impact on the resulting time-delay measurements when using an S-wave probe.

2.3 Loading Protocols

We repeat our experiments at five or six uniaxial loads for each sample and probe-type. A hydraulic press provided the load (Figure 1). The sample, along with spacers, is placed in the cell between two stainless steel plates to promote uniform load distribution. The press pistons apply a constant force with a sequence of hydraulics, with the applied load being this force divided by the sample area. We apply the load in steps: raise the force to have a 1 MPa load on the sample and collect data for both the P and S probes, then release the force, then raise the force to 2 MPa and record the next dataset, continue up to 15 MPa for Sample 1 and 18 MPa for Sample 2. The additional load for Sample 2 was necessary because of the reversal between 10 and 15 MPa. Although the steel plates help to distribute the strain uniformly throughout the sample, we do not expect
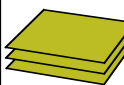
	Initial layer configuration	Applied load	PUMP source	P-probe	S-probe
Force direction	n/a	⬇	↔ y	↔ y	z ↕
propagation direction	n/a	n/a	x ↙	y →	y →
Sample 1 vertical		bow out	horizontal distortion	together and apart	slide vertically
Sample 2 horizontal		together	Horizontal distortion	Compression and dilation	vertical distortion

Figure 3. Schematic summary of the forces acting on layers within our samples. The top rows show force directions, with the thickness of the arrow indicating the different strengths of the forces (not to scale). The bottom two rows show the expected perturbations relative to the layering in each sample.

the strain to be uniform throughout. However, we do expect it to be distributed similarly at different loads and among different samples.

3 Theory and Modeling

3.1 Intuition

Figure 3 gives a schematic illustration of the expected sample responses to each type of applied force. Three forces act on the sample simultaneously: the static load, the PUMP wave, and the probe wave. Under a static load, we expect the layers in Sample 1 (with vertical layers) to bow out, while those in Sample 2 (with horizontal layers) will squeeze together. For the PUMP, we expect this perturbation to distort layers within the horizontal plane; several layers will distort together because the transducer diameter covers approximately 25 layers. For Sample 1, the layers are vertical, so the distortion is across the layers and would change their separation. For Sample 2, the distortion will remain largely within the horizontal layer itself. The P-probe will move Sample 1 layers closer and further together, but will compress/dilate within the Sample 2 layers. The S-probe will slide the layers against each other in Sample 1, but will vertically distort layers in Sample 2 (the transducer covers approximately ten layers).

3.2 Modeling the PUMP strain

We are interested in traveling waves because, in the field, transient signals are easier to excite than resonance modes. To achieve this in our experiments, we send only four cycles of the PUMP, and at a frequency such that this PUMP does not excite the entire sample simultaneously. As a result, our probes sense a much more complicated strain than what occurs in resonance-based DAET (Renaud et al. (2008)). To explore this further, we present a simple numerical model of the experiment, based on a finite-difference implementation of the elastic wave equation (Virieux, 1986; Graves, 1996) to determine what the probe senses as it travels across the sample. More details on the numerical results are given in Supplementary Text S5.

Our model estimates the cumulative strain, caused by the PUMP, that is sensed by the probe wave during our experiments. We simulate PUMP propagation and estimate the resulting strain distribution as a function of position in the sample and propagation time. Examples of strain field snapshots are shown in Figure 4.

We use calculated strains to compute the cumulative strain experienced by the probe as it travels across the sample, perpendicular to the PUMP propagation direction. In our experiments, we analyze only the arrival time of the probe, so we expect that the strain experienced by the first part of the probe waveform is most important. As a result, it is not necessary to model the probe propagation (see further discussion in Supplementary Text S5). Instead, we compute (analytically) where the probe wave will be within the PUMP strain field; these calculated locations are shown by white ellipses in Figure 4(b,c). To estimate the cumulative strain, we integrate the strain encountered by the probe over both space (within the white ellipse) and time (the white ellipse moves as the probe moves), and then divide by the path length. This follows a procedure identical to that used by Gallot et al. (2015) (more detail in Supplementary Text S5). The results of this calculation are shown in Figure 4(d), and demonstrate that the cumulative strain is at the frequency of the pump, and that it varies in magnitude (but not in frequency) as a function of the probe transmission delay.

3.3 Linking modulus to applied pressure

Rivière et al. (2016) introduce a simple model to fit the change in modulus to an exponential function of applied pressure. The change in modulus ($M = \rho v^2$), induced
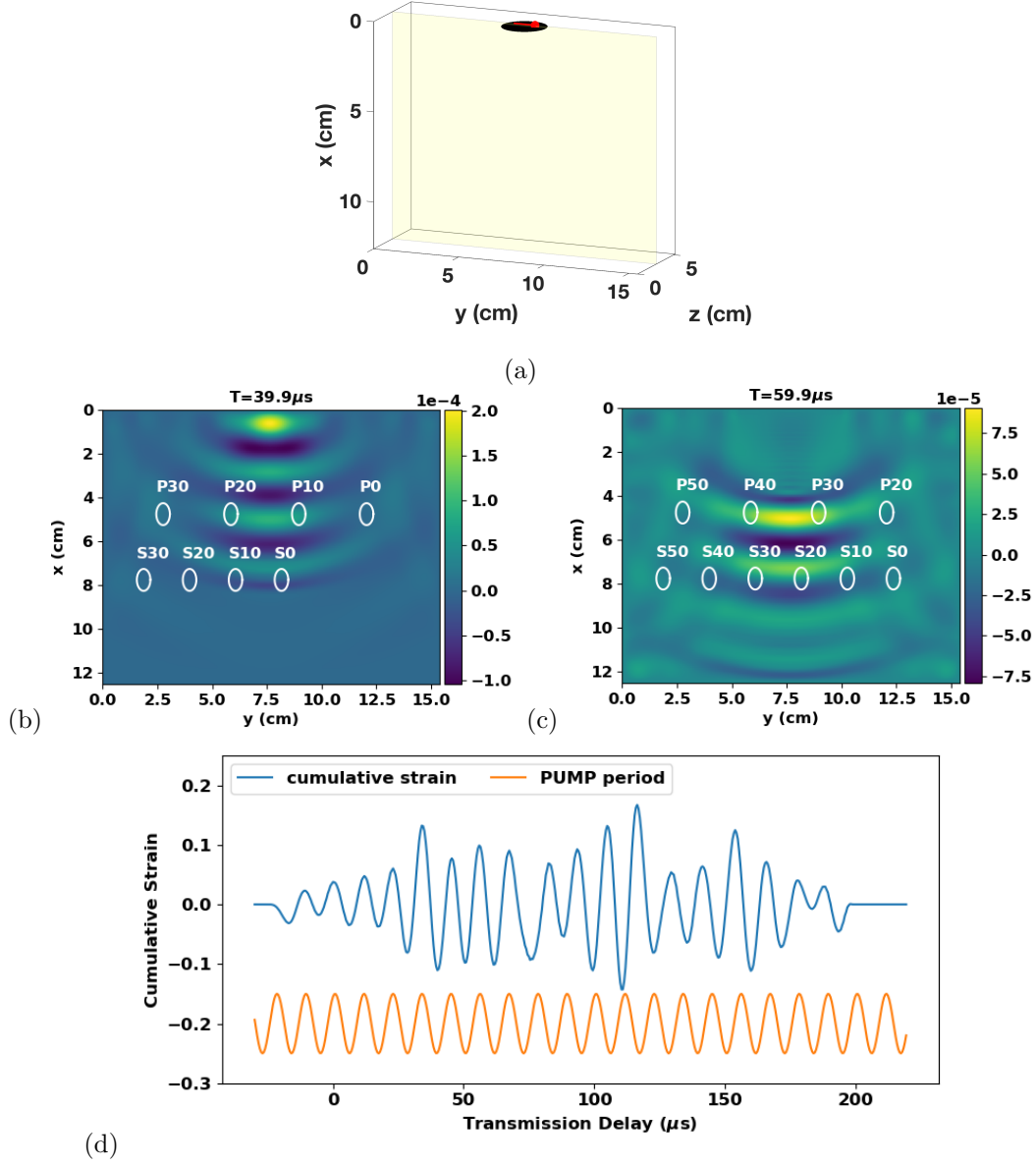
Figure 4. (a) Schematic depiction of the numerical model. The black area in the $y - z$ plane represents the location of the pump transducer, and example snapshots are taken in the $x - y$ plane. (b,c) Example snapshots of the ϵ_{yx} component of the strain. Labels in white indicate the wave type and the transmission delay (in μs), illustrating the locations of the P- and S-probe extents for various transmission delays. (d) Modeled cumulative total strain for the P-probe, estimated by integrating the PUMP strain along the probe path for different probe transmission delays. Component breakdowns and analyses for S-probe times are given in Supplementary Figures S5 and S6, respectively.

by the PUMP, can be recovered easily from the change in the traveltime of the probe wave via

$$\frac{\Delta M}{M} = \frac{2\rho v \Delta v}{M} = \frac{2\Delta v}{v} = 2\frac{\Delta T}{T} ,$$

where T is the travel time, v is the velocity and Δ indicates a change. Rivière et al. (2016) suggest simply fitting this change in modulus to an exponential model,

$$\frac{\Delta M}{M} = Ae^{-\frac{P}{P_0}} . \tag{1}$$

As mentioned above, we measure a change in traveltime (and thus modulus) for many different transmission delays. To reduce these data to a single number as a function of applied load, we extract the maximum traveltime delay (and thus change in modulus) for each applied load, and fit the resulting datasets to this simple model. This model is also used by Simpson et al. (2021) to fit velocity change data as a function of confining pressure.

4 Experimental Results

4.1 Velocities and Amplitudes

As a precursor to the nonlinear wave mixing data, we first assess changes in velocity, anisotropy, and PUMP amplitude with applied load (Figure 5).

We measure the travel times of four waves from which we obtain four velocities: v_{yy} (P-probe), v_{yz} (S-probe), v_{xy} (S-PUMP), and v_{xx} (P-wave generated by S-PUMP transducer). Yurikov et al. (2019) describe a similar methodology to that used here for measuring velocities, which is summarized in Supplementary Text S1. In Figure 5a, all measured velocities increase as a function of applied load, except for a slight decrease for Sample 1 velocities at low loads.

Anisotropies are calculated using the velocities shown in Figure 5a: the P-wave anisotropy is between the $x-$ and $y-$directions, whereas the S-wave anisotropy is between the yz and xy directions. Figure 5b shows that anisotropy is largest for P-waves in Sample 1. In that sample, the P-wave probe (v_{yy}) travels across the layering (the slow direction), whereas the S-wave excited by the PUMP transducer travels along the layers (the fast direction). This is expected based on prior reports by Gallot et al. (2015). All measures of anisotropy increase slightly and then plateau or decrease at higher applied loads. We note that different waves are measured with different transducers and frequencies in the

different directions, so conclusions about the absolute anisotropy of the samples should not be made with these data. However, we do not expect these errors to change with applied load. In addition, all changes are within the errors of our estimated velocities, so we cautiously conclude that anisotropy changes only by a few percent during our experiments.

Figure 5c shows the maximum value of the recorded PUMP signal, obtained using the dotted line setup in Figure 1. The maximum change in this amplitude is 20% for the P-wave probe in Sample 2. Note also that PUMP amplitude increases initially with applied load in Sample 2, whereas it decreases initially for Sample 1. Neither sample shows a consistent trend in PUMP amplitude with applied load.

To summarize, with the exception of the PUMP amplitude for the first step in load (from 1 to 2 MPa), the applied load changes velocity, anisotropy and PUMP amplitude by only a few percent.

4.2 Nonlinear Responses

For each sample and applied load, we performed two kinds of nonlinear wave-mixing experiments: P-wave probe, and S-wave probe. Figure 6 shows measured travel time delays (in ns) as a function of the transmission delay time (in μs) between when the PUMP and probe waves were initiated. (Recall from Section 3.3 that the travel time delay can be related directly to changes in moduli.) We note that some of these data were part of the conference presentation of (Hayes et al., 2018).

In Figure 6 – and as illustrated in the cartoon in Figure 2(c) – we see two clear frequency components in the time delay vs transmission delay data (as reported in similar experiment designs (Gallot et al., 2015; TenCate et al., 2016)). The first component follows the total envelope of the PUMP wave pulse, while the second higher-frequency component matches the period of the PUMP wave (90 kHz).

It is the component due to the PUMP envelope that explains why there is a net rise in time delay with transmission delay for some PUMP/probe combinations, while others show a decrease (compare Figure 6(a) and (b)). Whether the probe senses the increasing or decreasing part of the PUMP envelope depends largely on sample geometry and the relative locations of the PUMP and probe transducers. Thus, (a) shows the on-
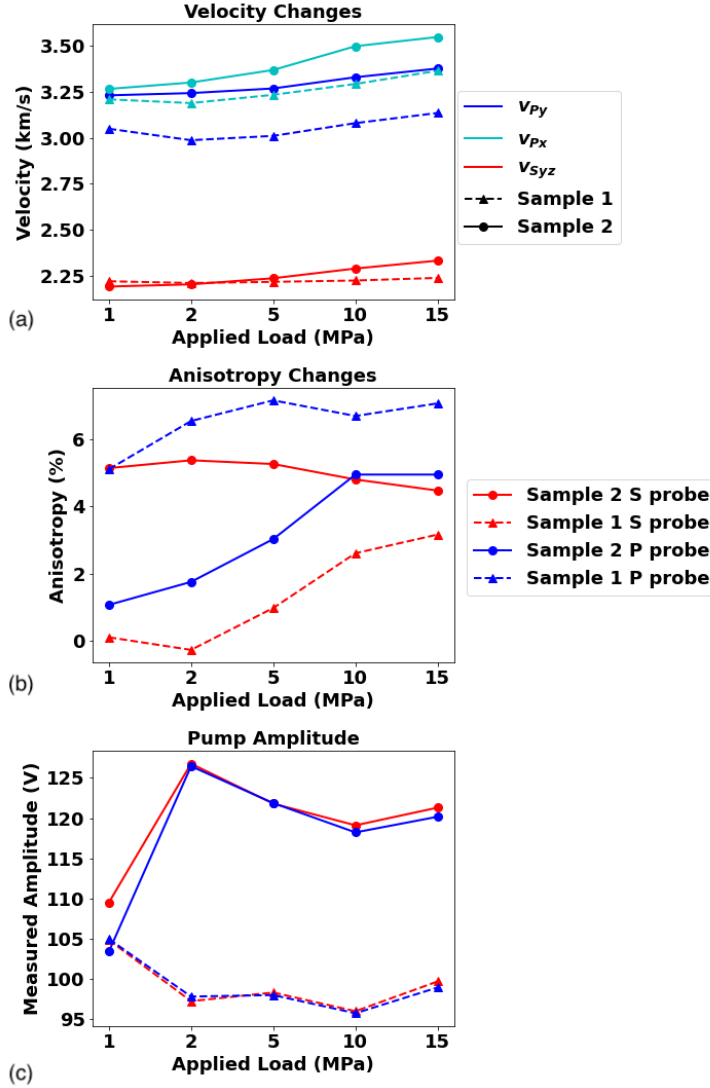
Figure 5. Comparison of (a) velocity, (b) anisotropy, and (c) recorded PUMP amplitude with applied load. (a) All measured velocities increase as a function of applied load, except for a slight decrease for Sample 1 velocities at low loads. (b) Anisotropy is most significant for P-waves in Sample 1, as expected. All measures of anisotropy increase slightly and then plateau or decrease at higher applied loads. Nevertheless, all are within the errors of the estimated velocities. (c) PUMP amplitude differences are quite consistent on the same sample (with different probes), but evolve quite differently as a function of load between the two samples. Overall, the amplitude changes are 9-20% of the average PUMP amplitude. The legend in (b) also applies to (c).
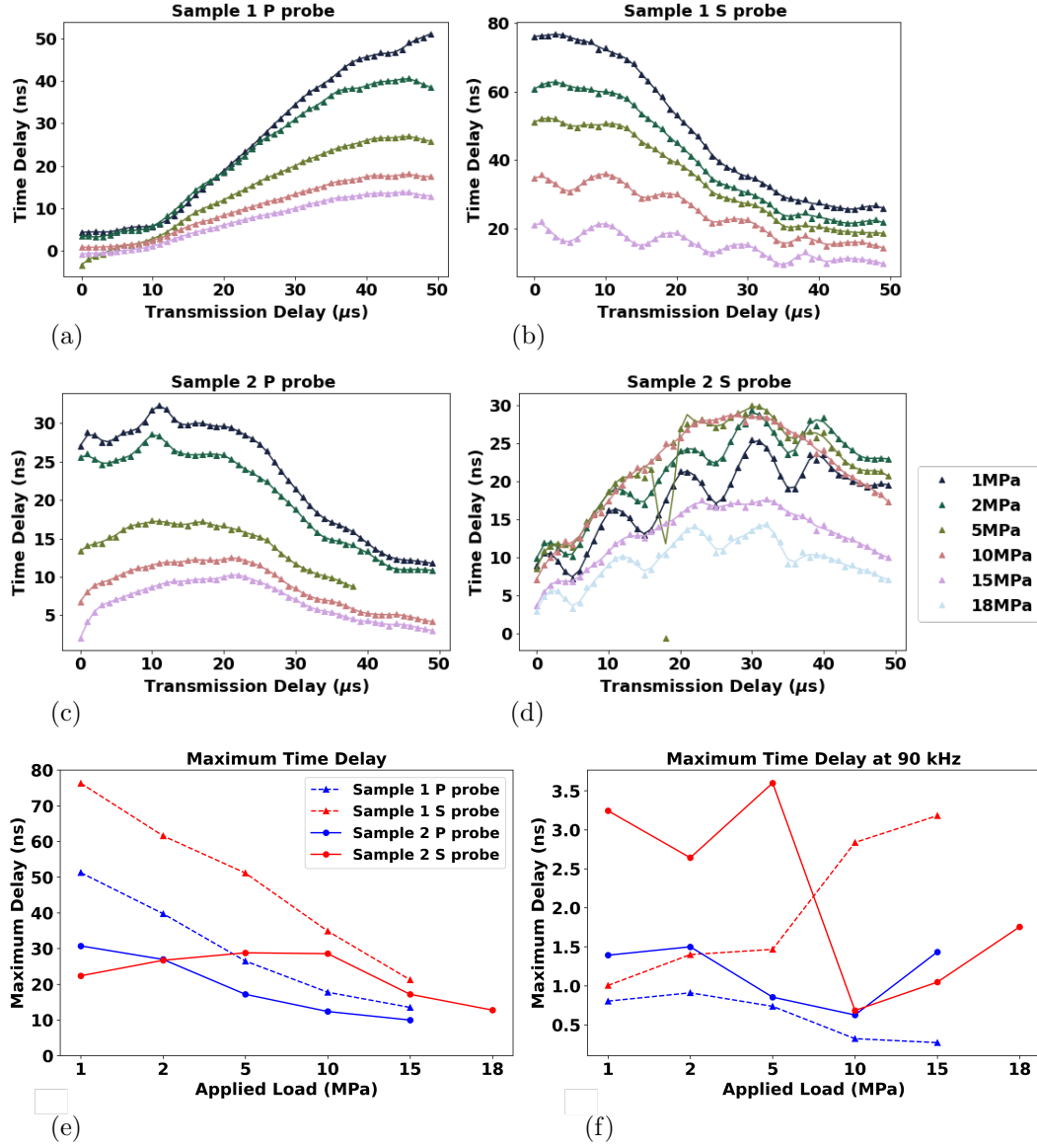
Figure 6. Time delay vs. transmission delay time data for different applied loads. (a) Sample 1 (vertical layers) with a P-probe, (b) Sample 1 with an S-probe, (c) Sample 2 (horizontal layers) with a P-probe, (d) Sample 2 with an S-probe. Note that, with the exception of the data in (d), the delay time decreases with applied load. (e) The maximum delay time as a function of applied load. (f) The maximum of the 90 kHz signal component as a function of applied load.

set of the PUMP/probe interaction, whereas (b) shows the tail-end of the interaction as the PUMP pulse passes out of the interaction region in the center of the sample. We note that it is this envelope part of the time delay vs transmission delay data that TenCate et al. (2016) found to change with sample orientation.

For the second, higher-frequency component, we compute the maximum of this 90 kHz component by filtering the travel time delay data with a butterworth bandpass filter (corner frequencies 50 and 150 kHz), and then record the maximum of the filtered signal. Our results show that there is no consistent trend in this 90 kHz component; previous work has also shown this component to be independent of sample orientation (TenCate et al., 2016). What controls the signal at 90 kHz remains an open question.

In summary, the envelope of the travel time delays decrease as a function of applied load for all experiments, except for the S-probe in Sample 2.

4.3 Fitting to the model

To conclude this section, we fit the data in Figure 6(e) to the model given in the Theory section in equation 1. The results of this fitting are shown in Figure 7. For Sample 2 with the S-probe, we note that there is no modulus change before 10 MP; thus, we include only 10, 15, 18 MPa in the fit. We show the characteristic load for each probe and sample type as insets in Figure 7; these are consistent within our experimental errors. The values agree with those recovered by Rivière et al. (2016) on sandstones, but they are different from those recovered by Simpson et al. (2021) for metamorphic rocks.

5 Discussion

Before interpreting new observations from our data, we first discuss how our data agree with known results. We observe that the nonlinear response changes by a factor of three to five, whereas the changes in velocities are on the order of at most ten percent. Scalerandi et al. (2018), among many others, observe that the nonlinear response to fractures is generally larger than the linear response, consistent with our observations. Our Sample 1 has larger delays than Sample 2 (Figures 6); this is consistent with the observations of TenCate et al. (2016), who find that the relative orientations of PUMP, probe, and sample layering influence the magnitude of the measured traveltime delays. TenCate et al. (2016) also note, as do we (Figure 6(f)), that there was no change in the
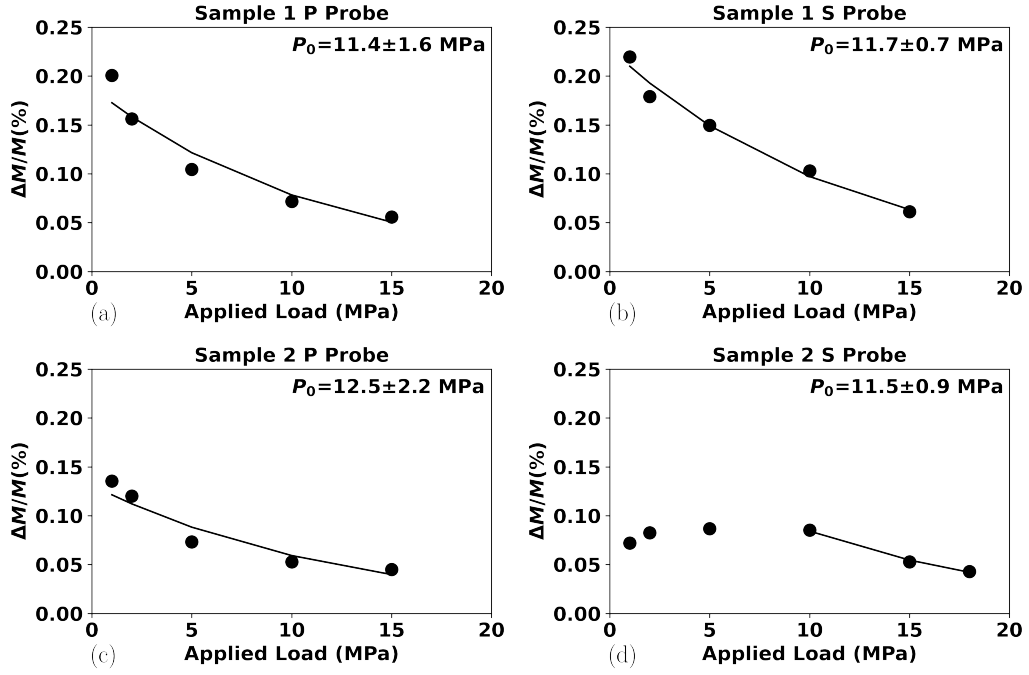
Figure 7. Fits to the model in equation 1 for (a) Sample 1 (vertical layers) with a P-probe, (b) Sample 1 with an S-probe, (c) Sample 2 (horizontal layers) with a P-probe, and (d) Sample 2 with an S-probe. For all cases, the characteristic load P_0 (insets) is the same within error.

higher-frequency (90 kHz) component of the time delay signal when changing the orientation of the samples.

Our main new observation from these data is that, with the exception of the first three loads for Sample 2 with an S-probe, the nonlinear signal decreases with applied load. This decrease is well-described by an exponential decay with an average characteristic load of 11.8±1 MPa across the four experiments. These results are consistent with published results using confining pressure (Rivière et al., 2016) instead of our uniaxial load. (Note that Zinszner et al. (1997) also see a significant drop in the nonlinear signal near 10 MPa.) We posit that this signal decrease with applied load is controlled by cracks or other grain-scale structures aligned with the visible layering in the sample. Before going into the details of this interpretation, we first rule out two other possible mechanisms.

Bittner and Popovics (2019) show that fluid movement occurs during a nonlinear resonant ultrasound spectroscopy (NRUS) experiment. The applied loads here are not large enough to limit pore-scale flow (Gist (1994) find that 40 MPa is sufficient to limit some pore-scale flow), and so we cannot immediately rule out the movement of water as a significant mechanism in our results. That said, at ambient load conditions Khajehpour Tadavani et al. (2020) find that it takes many days for changes in fluid content to show similar magnitude changes as those observed here. This leads us to conclude that changes in ambient humidity are unlikely to be the controlling mechanism behind our results.

Another potential mechanism to explain our results is that the sample may change length due to either the PUMP wave or the applied load. (TenCate et al., 2016) note that strains on the order of 10^{-4} would be necessary to explain their data based on changes in length due to the PUMP; they also note that travel time delays would also be observed in linear materials, which they show is not the case. If changes in length were to explain our signals, we would expect the maximum travel time delay to increase with applied load as the sample would get longer in both the PUMP and probe propagation directions. This is counter to our observations. We thus exclude changes in length as a possible mechanism.

Having ruled out these two potential mechanisms controlling our nonlinear signal, we now interpret our results in terms of the changes in the layers, as sketched in Figure 3. We first examine what might be the small-scale structures that are present at the layer

boundaries. Benson et al. (2005) do interpret crack-like microstructures in rocks from the same quarry with the cracks aligned with the layers. It is well-established that cracks are a dominant influence on changes in velocity with applied load (Nur, 1971), and that cracks are a driver of nonlinearity (Guyer & Johnson, 1999, 2009). We do not think that we have applied enough stress to produce new cracks (which might increase nonlinearity, as seen in Sample 2 with the S-probe). For example, Browning et al. (2017) find that new cracks develop at a confining pressure of approximately 40 MPa, which is much higher than the 18 MPa of uniaxial load that we apply. Batzle et al. (1980) see distinct opening of vertical cracks at uniaxial loads up to 30 MPa. This leads us to expect that we could open vertical cracks in Sample 1. However, our results (Figure 6) do not show any increase in nonlinearity in Sample 1, even with low applied loads, meaning that they are not consistent with a 'crack-opening' interpretation.

Our data suggest that the underlying mechanism is perhaps less sensitive to the orientation of the microstructures than to how much strain is required to perturb these structures. If the mechanism depended on the orientation of the structures, then we would expect different responses for samples with that micro-structure oriented in different ways (i.e., Sample 1 vs Sample 2). In contrast, the stiffness of the contacts is likely to increase as the load is increased, independent of the orientation of the layers. As the contacts get stiffer, it is logical that they will not be as easily perturbed by the PUMP wave, thus decreasing the nonlinear response. Our only observation that is not consistent with this explanation is that, for Sample 2 and the S-probe, the decay does not begin until a larger load. This is puzzling, yet it also shows consistency with Simpson et al. (2021), where they observe this kind of holding before changes with (in their case) confining pressure. It is interesting that once the decay begins it proceeds with the same characteristic load.

As a final observation from our data, we check their consistency with the postulation by Rivière et al. (2015) that there are two clear mechanisms causing changes to the nonlinear response. This observation is also discussed by Scalerandi et al. (2015), where they divide these mechanisms into clapping and hysteresis. Our results are consistent with the presence of two mechanisms. The first mechanism, characterized by the signal at the frequency of the PUMP, seems independent of the applied load (Figure 6f), and crack orientation (TenCate et al., 2016). The second mechanism, which follows the shape of the envelope of the PUMP signal depends strongly on load and crack orientation (Figure 6a).

6 Conclusions

We present a dataset showing the evolution of the nonlinear interaction of different wave-types as a function of applied uniaxial load. We find a characteristic load that is consistent with literature results for other samples measured with different experimental configurations. Our data support the idea that nonlinear measurements are more sensitive to aligned structures (such as cracks or layering) – and their changes to these aligned stuctures – than other (linear) measurements used to characterize the sample. This is supported by a larger percentage change in moduli, when compared to directly measured changes in wavespeed, anisotropy, and amplitude of the perturbing PUMP wave.

7 Open Data

Data are published as (Malcolm & Poduska, 2021), available via the Memorial Dataverse repository, under the Creative-Commons CC0 licence. Figures were generated with Matplotlib version 3.2.2 (DOI:10.5281/zenodo.4030140) and other data processing was done with numpy (Harris et al., 2020), version 1.19.1 and scipy (Virtanen et al., 2020) version 1.7.2.

References

Alkhalifah, T., & Tsvankin, I. (1995). Velocity analysis for transversely isotropic media. *Geophysics*, *60*(5), 1550–1566.

Aoki, Y. (2015). Monitoring temporal changes of seismic properties. *Frontiers in Earth Science*, *3*, 42.

Asaka, M., Luo, M., Yamatani, T., Kato, A., Yoshimatsu, K., & Knapp, L. (2018). 4D seismic feasibility study: The importance of anisotropy and hysteresis. *The Leading Edge*, *37*(9), 688-698. Retrieved from `https://doi.org/10.1190/tle37090688.1` doi: 10.1190/tle37090688.1

Batzle, M., Simmons, G., & Siegfried, W. (1980). Microcrack closure in rocks under stress: Direct observation. *Journal of Geophysical Research*, *85*, 7072–7090.

Benson, P., Meredith, P., Platzman, E., & White, R. (2005, oct). Pore fabric shape anisotropy in porous sandstones and its relation to elastic wave velocity and permeability anisotropy under hydrostatic pressure. *International Journal of Rock Mechanics and Mining Sciences*, *42*(7-8), 890–899. Retrieved from `http://linkinghub.elsevier.com/retrieve/pii/S1365160905000705` doi: 10.1016/j.ijrmms.2005.05.003

Birch, F. (1960). The velocity of compressional waves in rocks to 10 kilobars, part 1. *Journal of Geophysical Research*, *65*(4), 1083–1102. Retrieved from `http://onlinelibrary.wiley.com/doi/10.1029/JZ065i004p01083/full`

Bittner, J., & Popovics, J. S. (2019). Direct imaging of moisture effects during slow dynamic nonlinearity. *Applied Physics Letters*, *114*(2), 021901.

Broda, D., Staszewski, W., Martowicz, A., Uhl, T., & Silberschmidt, V. (2014). Modelling of nonlinear crack–wave interactions for damage detection based on ultrasound—a review. *Journal of Sound and Vibration*, *333*(4), 1097–1118.

Browning, J., Meredith, P. G., Stuart, C. E., Healy, D., Harland, S., & Mitchell, T. M. (2017). Acoustic characterization of crack damage evolution in sandstone deformed under conventional and true triaxial loading. *Journal of Geophysical Research: Solid Earth*, *122*(6), 4395–4412. doi: 10.1002/2016JB013646

Catheline, S., Wu, F., & Fink, M. (1999, May). A solution to diffraction biases in sonoelasticity: The acoustic impulse technique. *The Journal of the Acoustical Society of America*, *105*(5), 2941–50. Retrieved from `http://www.ncbi.nlm.nih`

`.gov/pubmed/10335643`

Gallot, T., Malcolm, A. E., Szabo, T. L., Brown, S., Burns, D., & Fehler, M. (2015). Characterizing the nonlinear interaction of S- and P-waves in a rock sample. *Journal of Applied Physics*, *117*, 034902.

Gist, G. (1994). Fluid effects on velocity and attenuation in sandstones. *The Journal of the Acoustical Society of America*, *96*(2), 1158–1173. Retrieved from `http://scitation.aip.org/content/asa/journal/jasa/96/2/10.1121/1.410389`

Graves, R. W. (1996). Simulating seismic wave propagation in 3d elastic media using staggered-grid finite differences. *Bulletin of the Seismological Society of America*, *86*(4), 1091–1106.

Guyer, R. A., & Johnson, P. A. (1999). Nonlinear Mesoscopic Elasticity: Evidence for a New Class of Materials. *Physics Today*, *52*(4), 30. Retrieved from `http://scitation.aip.org/content/aip/magazine/physicstoday/article/52/4/10.1063/1.882648` doi: 10.1063/1.882648

Guyer, R. A., & Johnson, P. A. (2009). *Nonlinear mesoscopic elasticity: The complex behaviour of rocks, soil, concrete.* John Wiley & Sons.

Harris, C. R., Millman, K. J., van der Walt, S. J., Gommers, R., Virtanen, P., Cournapeau, D., . . . Oliphant, T. E. (2020, September). Array programming with NumPy. *Nature*, *585*(7825), 357–362. Retrieved from `https://doi.org/10.1038/s41586-020-2649-2` doi: 10.1038/s41586-020-2649-2

Hayes, L., & Malcolm, A. (2017). How fracture orientation and particle motion impact nonlinear interactions in an elastic medium. *2017 SEG Technical Program Expanded Abstracts*, 1–5.

Hayes, L., Malcolm, A., Moravej, K., & Butt, S. (2018). Nonlinear interactions of P and S waves under uniaxial stress. *POMA proceedings of the 21st International Symposium on Nonlinear Acoustics*.

Hughes, D., & Kelly, J. (1953). Second-order elastic deformation of solids. *Physical Review*, *89*(1940). Retrieved from `http://adsabs.harvard.edu/abs/1953PhRv...92.1145H`

Khajehpour Tadavani, S., Poduska, K. M., Malcolm, A. E., & Melnikov, A. (2020). A non-linear elastic approach to study the effect of ambient humidity on sandstone. *Journal of Applied Physics*, *128*(24), 244902.

Lott, M., Payan, C., Garnier, V., Vu, Q. A., Eiras, J. N., Remillieux, M. C., . . . Ulrich, T. (2016). Three-dimensional treatment of nonequilibrium dynamics and higher order elasticity. *Applied Physics Letters*, *108*(14), 141907.

Lott, M., Remillieux, M. C., Garnier, V., Le Bas, P.-Y., Ulrich, T. J., & Payan, C. (2017). Nonlinear elasticity in rocks: A comprehensive three-dimensional description. *Physical Review Materials*, *1*(2), 023603. Retrieved from `http://link.aps.org/doi/10.1103/PhysRevMaterials.1.023603` doi: 10.1103/PhysRevMaterials.1.023603

Lott, M., Remillieux, M. C., Le Bas, P.-Y., Ulrich, T. J., Garnier, V., & Payan, C. (2016). From local to global measurements of nonclassical nonlinear elastic effects in geomaterials. *Journal of the Acoustical Society of America*, *140*(EL231). Retrieved from `http://dx.doi.org/10.1121/1.4962373` doi: 10.1121/1.4962373

Malcolm, A., & Poduska, K. (2021). *Nonlinear Wave Mixing as a Function of Applied Load.* Scholars Portal Dataverse. Retrieved from `https://doi.org/10.5683/SP3/CZXST1` doi: 10.5683/SP3/CZXST1

Muir, T. G., Cormack, J. M., Slack, C. M., & Hamilton, M. F. (2020). Elastic softening of sandstone due to a wideband acoustic pulse. *The Journal of the Acoustical Society of America*, *147*(2), 1006–1014.

Norris, A., & Johnson, D. (1997). Nonlinear elasticity of granular media. *Journal of . . .*, *64*(March), 39–49. Retrieved from `http://appliedmechanics.asmedigitalcollection.asme.org/article.aspx?articleid=1412558`

Nur, A. (1971). Effects of stress on velocity anisotropy in rocks with cracks. *Journal of Geophysical Research*, *76*(8), 2022–2034. Retrieved from `http://doi.wiley.com/10.1029/JB076i008p02022` doi: 10.1029/JB076i008p02022

Ostrovsky, L., & Johnson, P. (2001). Dynamic nonlinear elasticity in geomaterials. *Rivista del nuovo cimento*, *24*(7). Retrieved from `http://lanl.gov/orgs/ees/ees11/geophysics/nonlinear/2001/LaRivista.pdf`

Remillieux, M. C., Ulrich, T. J., Goodman, H. E., & Ten Cate, J. A. (2017). Propagation of a Finite-Amplitude Elastic Pulse in a Bar of Berea Sandstone: A Detailed Look at the Mechanisms of Classical Nonlinearity, Hysteresis, and Nonequilibrium Dynamics. *Journal of Geophysical Research: Solid Earth*, *122*(11), 8892–8909. doi: 10.1002/2017JB014258

Renaud, G., Calle, S., Remenieras, J. P., & Defontaine, M. (2008, July). Exploration of trabecular bone nonlinear elasticity using time-of-flight modulation. *IEEE transactions on ultrasonics, ferroelectrics, and frequency control*, *55*(7), 1497–507. Retrieved from `http://www.ncbi.nlm.nih.gov/pubmed/18986939` doi: 10.1109/TUFFC.2008.825

Renaud, G., Le Bas, P.-Y., & Johnson, P. A. (2012, June). Revealing highly complex elastic nonlinear (anelastic) behavior of Earth materials applying a new probe: Dynamic acoustoelastic testing. *Journal of Geophysical Research*, *117*(B6), B06202. Retrieved from `http://doi.wiley.com/10.1029/2011JB009127` doi: 10.1029/2011JB009127

Renaud, G., Talmant, M., Callé, S., Defontaine, M., & Laugier, P. (2011, December). Nonlinear elastodynamics in micro-inhomogeneous solids observed by head-wave based dynamic acoustoelastic testing. *The Journal of the Acoustical Society of America*, *130*(6), 3583–9. Retrieved from `http://www.ncbi.nlm.nih.gov/pubmed/22225015` doi: 10.1121/1.3652871

Rivière, J., Pimienta, L., Scuderi, M., Candela, T., Shokouhi, P., Fortin, J., . . . Johnson, P. A. (2016). Frequency, pressure, and strain dependence of nonlinear elasticity in Berea Sandstone. *Geophysical Research Letters*, *43*(7), 3226–3236.

Rivière, J., Renaud, G., Guyer, R. A., & Johnson, P. A. (2013). Pump and probe waves in dynamic acousto-elasticity: Comprehensive description and comparison with nonlinear elastic theories. *Journal of Applied Physics*, *054905*, 1–19. Retrieved from `http://scitation.aip.org/content/aip/journal/jap/114/5/10.1063/1.4816395`

Rivière, J., Shokouhi, P., Guyer, R. A., & Johnson, P. A. (2015). A set of measures for the systematic classification of the nonlinear elastic behavior of disparate rocks. *Journal of Geophysical Research: Solid Earth*, *120*(3), 1587–1604.

Rusmanugroho, H., Darijani, M., & Malcolm, A. (2020). A numerical model for the nonlinear interaction of elastic waves with cracks. *Wave Motion*, *92*, 102444. doi: https://doi.org/10.1016/j.wavemoti.2019.102444

Scalerandi, M., Bentahar, M., & Mechri, C. (2018). Conditioning and elastic nonlinearity in concrete: Separation of damping and phase contributions. *Construction and Building Materials*, *161*, 208-220. Retrieved from `https://`

`www.sciencedirect.com/science/article/pii/S0950061817322481`   doi: https://doi.org/10.1016/j.conbuildmat.2017.11.035

Scalerandi, M., Idjimarene, S., Bentahar, M., & El Guerjouma, R. (2015). Evidence of microstructure evolution in solid elastic media based on a power law analysis. *Communications in Nonlinear Science and Numerical Simulation*, *22*(1-3), 334–347.

Sens-Schönfelder, C., & Eulenfeld, T. (2019). Probing the in situ elastic nonlinearity of rocks with earth tides and seismic noise. *Physical review letters*, *122*(13), 138501.

Sens-Schönfelder, C., Snieder, R., & Li, X. (2018). A model for nonlinear elasticity in rocks based on friction of internal interfaces and contact aging. *Geophysical Journal International*, *216*(1), 319–331.

Simpson, J., van Wijk, K., & Adam, L. (2021). Spatial dependence of dynamic nonlinear rock weakening at the alpine fault, new zealand. *Geophysical Research Letters*, e2021GL093862.

TenCate, J. A., Malcolm, A. E., Feng, X., & Fehler, M. C. (2016). The effect of crack orientation on the nonlinear interaction of a P wave with an S wave. *Geophysical Research Letters*, *43*(12), 6146-6152. Retrieved from `https://agupubs.onlinelibrary.wiley.com/doi/abs/10.1002/2016GL069219`   doi: 10.1002/2016GL069219

Virieux, J. (1986). P-sv wave propagation in heterogeneous media; velocity-stress finite-difference method. *Geophysics*, *51*(4), 889–901.

Virtanen, P., Gommers, R., Oliphant, T. E., Haberland, M., Reddy, T., Cournapeau, D., ... SciPy 1.0 Contributors (2020). SciPy 1.0: Fundamental Algorithms for Scientific Computing in Python. *Nature Methods*, *17*, 261–272. doi: 10.1038/s41592-019-0686-2

Wang, Q.-Y., Campillo, M., Brenguier, F., Lecointre, A., Takeda, T., & Hashima, A. (2019). Evidence of changes of seismic properties in the entire crust beneath Japan after the Mw 9.0, 2011 Tohoku-Oki earthquake. *Journal of Geophysical Research: Solid Earth*.

Yurikov, A., Nourifard, N., Pervukhina, M., & Lebedev, M. (2019). Laboratory ultrasonic measurements: Shear transducers for compressional waves. *The Leading Edge*, *38*(5), 392–399.

Zinszner, B., Johnson, P., & Rasolofosaon, P. (1997). Influence of change in physical state on elastic nonlinear response in rock: Significance of effective pressure and water saturation. *Journal of Geophysical Research*, *102*(96), 8105–8120. Retrieved from `http://onlinelibrary.wiley.com/doi/10.1029/96JB03225/ full`

Supporting Information for "Experimental Monitoring of Nonlinear Wave Interactions Under Uniaxial Load"

Alison Malcolm [1], Lauren Hayes[1], Kamal Moravej[1], Andrey Melnikov[1],

Kristin Poduska[3], Stephen Butt[2]

[1]Department of Earth Sciences, Memorial University of Newfoundland

[2]Department of Engineering, Memorial University of Newfoundland

[2]Department of Physics and Physical Oceanography, Memorial University of Newfoundland

Contents of this file

Introduction

This supporting information gives additional detail on the experimental setup not necessary for understanding the results, but necessary for duplicating the experiments. In addition, it gives more detail on the modeling of the strain induced by the pump and the cumulative strain observed by the probe.

Text S1: Measuring Velocity at Different Loads

It is important to calibrate transducers to have accurate travel time measurements by

————

December 2, 2021, 10:14am

measuring the travel time through different thicknesses of the same material and finding the intercept time. This intercept time measures the inherent delay from the transducer. For our transducers this number is 0.3 μs for S and 0.5 μs for P; we apply these corrections to the measured travel times before computing the associated velocities. To measure the velocities shown in Table 1 and Figure 5, we first pick the travel times. For the lowest applied load (1 MPa), this is done by picking the zero-crossing before the peak within a user-defined time window. Each pick is then manually checked to ensure that it chose the correct arrival. For higher loads, we measure the travel time change by cross-correlating the waveforms with those recorded at 1 MPa. When we extract the P-wave velocity from measurements of the S-wave PUMP, we are using what are sometimes referred to as parasitic P-waves, generated by S-wave transducers. In this case, the P-wave is much smaller than the S-wave and so to recover a reliable velocity change we window the data to include only the P-wave. This methodology along with estimates of the errors in P-wave velocities inferred from such parasitic waves is described by Yurikov et. al. (2019); they report errors of 5% compared with traditional methods of measuring P-wave velocities with P-wave transducers. We do not need to window when measuring the S-wave travel time because the S-wave is much stronger. For measurements on the probe signals, we record only about 2 periods of the signal and so there is no interference between different wavetypes. We measure the dimensions of the samples with calipers and use them to convert the travel times to velocities; these values are given in Table 1. We use the repeated measurements on the PUMP signals (for the two probes) to estimate the errors in our recovered velocities at less than 5%, in line with the errors from Yurikov et al. (2019) from using parasitic P-waves from S-transducers.

Text S2: Experimental details

All signals are generated with a standard (Agilent 33500B Series) function generator and recorded with a standard (KEYSIGHT InfiniiVision MSOX2014A) 8-bit oscilloscope. The pump signals are amplified with an (E & I 240L RF) power amplifier and all recorded signals are high-pass filtered with a (Krohn-Hite) adjustable digital filter with cut-off frequency of 600 kHz. Each recorded signal is an average of 4096 signals to reduce noise and sampled every 4 ns; example signals are shown in Figure 2. The signals are recorded at the lowest vertical range on the oscilloscope that does not result in clipping the recorded signal, this maximizes the accuracy of the recorded probe signal. This ranges from 1-200 mVp-p, except for when we record the PUMP alone (dotted lines in Figure 1) where the scale is 150 Vp-p.

We use Olympus transducers, specifically V-153 (S, 1 MHz, 1.3 cm diameter), V-103 (P, 1 MHz, 1.3 cm diameter) for the two probes and the V-1548 (S, 100 kHz, 2.5 cm diameter) for the PUMP. The driving frequencies of all transducers are chosen to give a signal recorded on the opposite face that most closely resembles our ideal waveform. For the pump this is a four-cycle sinusoid, and for the probe this is a one-cycle sinusoid. Example signals are shown in Figure 2.

All of our experiments were performed at room conditions, in an interior climate-controlled room. We wrapped the sample in plastic wrap to diminish the influence of humidity changes on the results. We would certainly expect to see changes in that environment over the course of the experiments, and the local humidity over the period of the experiment averaged 83% with significant excursions to a high of 100% and low of approximately 40%, with all days averaging between 75 and 95% and no consistent trends.

December 2, 2021, 10:14am

Experiments were completed on each sample and probe before moving to the next to minimize the effect of variations in room conditions on the results. Khajehpour Tadavani et. al. (2020) find that humidity changes impact the results, but that these impacts have an exponential time constant on the order of days to weeks for these samples, in other words these changes happen slowly compared to our experimental time.

Text S3: Measuring the strain This strain is measured using a laser-doppler vibrometer and averaging the amplitude (measured from the peak of the Hilbert transform of the signal) of the recorded particle velocity signals at several locations on the sample. We then divide the recorded particle velocity by the phase velocity of the recorded wave. This gives an estimate of the strain assuming that we are exciting plane waves. Because this assumption is not strictly true, we are confident only that this gives us the order-of-magnitude of the strain and that it gives us a good measure of the relative magnitude of the two strains. This is the same protocol as used by Gallot et al. (2015), repeated on this sample in our laboratory. It is explained in more detail by Khajehpour Tadavani et al. (2020).

Text S4: Computing the travel time delays We compute the travel time delays plotted on the y-axis in Figure 6 by fitting a sinc function to the five points nearest the peak of the cross-correlation of the two signals. This follows the suggestion of e.g. Catheline et al. (1999), replacing the parabola with a sinc function because in fitting the peak we are essentially assuming that we have undersampled our signals, for which a sinc interpolation is the optimal solution (Ali Gholami, personal communication, 2018). Our numerical experiments using one-cycle sine waveforms shifted by a known amount indicate that we can estimate a travel time delay with two digits of accuracy down to

approximately 1/100 of our sampling interval (i.e. the error in our travel time estimate is 0.04 ns).

Text S5: Modeling Strain

The goal of this section is to explain what our measurements are sensitive to. More specifically, we aim to demonstrate which parts of the pump waveform cause the perturbations we observe when we measure delays in the travel time of the probe wave. To this end, we model both waveforms through a sample that is meant to be close to both of the samples used in the experiment. The parameters of the model rock are given in Table S1. The code we use is a standard staggered-grid finite-difference algorithm (Virieux, 1986; Graves, 1996). The numerical parameters are given in table S2. This code computes the particle velocity and stresses; we compute the strain from the stresses using a linear Hooke's law. We use reflecting boundaries on all sides. Our goal is to estimate the cumulative strain, caused by the pump, that is sensed by the probe wave during our experiments. To this end, we show the results of three experiments. The first simulation is to verify the accuracy of our transducer model. This simulation is compared with a separate set of experimental data to verify that our modeled transducer does indeed agree with our experimental equipment, and uses a grid and geometry, described below, appropriate to that experiment. The second dataset we compute models the probe, which uses a fine mesh and a scaled-down model because of the higher frequency of the probe signal. This simulation is used to verify that our assumptions about where this signal is in space and time are accurate. The third experiment models the propagation of the pump. We first use these simulated data to compare with our experimentally recorded pump signal and evaluate the accuracy of the numerical model. We then use this simulation to estimate

the observed strain distribution in the sample for a variety of pump/probe delays from which we estimate the cumulative strain the probe wave will see as it travels across the sample. This simulation is done on a coarser grid and thus we are able to simulate the wave propagation throughout the larger sample.

We begin by checking the transducer model. We model the source transducer as a set of 492 point-forces distributed over a circular region on one face of the model. We do not weight the sources in any way, so all contribute equally to the generated waves. To verify that this is sufficiently accurate, we compare our modeled transducer radiation pattern with a recorded radiation pattern. The relevant numerical parameters are given in table S2. The experimental dataset that we compare to is measured in a homogeneous plexiglas sample. The experimental geometry is shown in Figure S1. We send a single cycle of a 200 kHz sine function to the source P-wave transducer (the same make and model as that used as the P-wave probe source in our other experiments) in the positive y-direction, and a laser doppler-interferometer measures the same y-component of the particle velocity on the opposite side of the sample. The experimental data are collected on a line and then corrected for geometrical spreading to recover the radiation pattern. For the numerical data, we excite a y-direction force on a simulated transducer with radius of 5 mm to match our transducer's active radius. We then record the mdoel data on an array of detectors on a circle of radius 2 cm centered on the transducer center to avoid the need for a geometrical spreading correction. We see in Figure S1 that the agreement between the experimental and modeled data are excellent. We thus conclude that our transducer model is adequate for the probe transducer when it is driven at 200 kHz. We now must ask if this translates to our probe signal, which is at a higher frequency. Although the only

way to know for certain is to do the experiment, the transducer is designed to respond linearly over a relatively wide frequency range, and so we do not anticipate significant deviations. For the PUMP signal, the argument is similar. It is a different transducer and different frequency range, but manufactured by the same company using the same technology. We thus expect that this model is sufficient for our purposes. In addition, this is the same modeling strategy and code used by Gallot et al. (2015) where they were able to obtain excellent agreement between the signal recorded with the laser on the surface (though they did not look at this agreement as a function of position).

Next, we look at the propagation of the probe. This is expected to be quite straight-forward as it is a small wave, likely in the linear regime, and it propagates directly from the source transducer to an identical receiver transducer on the opposite face. Because of the high-frequency of this signal, this simulation requires a small spatial sampling interval, which can be challenging numerically as it takes a great deal of memory to run the simulation. To mitigate these extreme memory requirements, we reduce the size of the model to be only $5 \times 15 \times 5$ cm in x, y, z, as shown in Figure S2. This will not result in an accurate waveform for the parts of the wave that arrive after the direct arrival as the scattering from the boundaries is significantly enhanced in this smaller simulation, but this scattering will not affect the direct arrival that we are interested in. Snapshots of the wavefield at several times are shown in Figure S2. On top of these snapshots, we plot an ellipse with major axis the size of the transducer and minor axis one wavelength. We also show, with two horizontal lines, the extent of the transducer. We assume that the transducer will measure only those signals that arrive between these two white lines. In what follows, we will use the pump strain within this ellipse to calculate the cumulative

strain that the probe sees as it travels across the sample. We see that the ellipse tracks

this first-arriving wave across the sample and includes the dominant part of the signal.

Little difference is anticipated if we change the details of the shape or size of this elliptical

domain. We show the ϵ_{yy} component of the strain because this is the component that we

dominantly excite and observe for a P-wave travelling in the y-direction. Although the

shape of the strain changes if we look at different components, the extent and travel time

does not, so we do not expect significant changes to these ellipsoidal regions if we were to

look at different strain components.

Now that we have verified that we are able to simulate our transducer response and that

the simulated probe wave travels directly across the sample in a way that is easily tracked,

we now model the pump signal. Figure S3 shows the model setup and the modeled pump

signal recorded on virtual transducers located within the sample. The displayed signal is

the average of all of the signals recorded within the area of the transducer, which is set

to correspond with the physical transducer located on the bottom of the sample in the

physical experiment. Varying the number of recording locations within the transducer or

even looking at the response at a single detector has only a minor influence on the results.

We model the data at 100 kHz rather than the 90 kHz at which we drove the physical

transducer because the spectrum of the data (shown in Figure S3 for a recording from the

center of the sample in (x, z) and the bottom in x, specifically $(x, y, z)=(12.6, 7.5, 2.5)$ cm)

has a spectrum centered closer to 100 kHz than to 90 kHz. We show the modeled signal

at several depths because our model is linearly elastic whereas our sample exhibits both

nonlinearities and is clearly visco-elastic. In addition, the numerical boundary conditions

are not perfect and we model the edges as though they are perfectly flat surfaces, which

they are not. These effects combine to make the boundary reflections significantly stronger in the model than they are in the data. We conclude this by comparing the recorded data with the modeled data at both $x = 12.5$ cm and $x = 5.5$ cm. At $x = 12.5$ cm we would expect the experimental and modeled data to agree, but they clearly do not. The waves arrive at approximately the same time (there is no shift in the experimental data on this sub-plot), but do not have the same waveform. By contrast, when looking at the data at $x = 5.5$ cm the times do not agree as expected (the modeled data are shifted), but the waveform shapes are nearly identical. In the data at $x = 5.5$ cm, there is a clear boundary reflection arriving after the direct wave. These two waves would be expected to be on top of one another when the data are recorded directly on the boundary, which changes the shape of the modeled waveform. Based on this comparison, we conclude that the modeled data are giving a more complicated picture of the waveforms than are likely present in the physical experiment, but this picture still captures the majority of the phenomena of interest particularly away from the edges of the sample.

Having discussed the validity of the model, we now use it to track the cumulative strain. This follows a procedure identical to that in (Gallot et al., 2015), which we describe briefly here. We model the strain caused by the pump, snapshots of the ϵ_{xy} component are shown in Figure S4, with the locations of the P- and S-probes overlain for various transmission delays. Using these snapshots, we then compute the cumulative strain for the AB-component of strain, ϵ_{AB}

$$e_{AB}^{cum}(\tau) = \frac{1}{|S|} \int_S \int_0^{T_{max}} \chi(x, t - \tau)\epsilon_{AB}(x, t)dxdt \tag{S.1}$$

where S is the path along which the probe travels, $|S|$ is its length, and χ is an indicator function that is equal to one in the vicinity of the probe wave and zero elsewhere. We

compute this cumulative strain for a range of phase shifts, τ, covering the range that we use in the experiments and more, and use strains up to a time of $T_{max} = 200$ μs, which is approximately the time it takes the pump wave to travel across the sample and then back to the source. Our procedure is to take the computed $\epsilon_{AB}(x, t)$ from the pump propagation and then multiply it by $\chi(x, t - \tau)$, where χ is supported (=1) on the ellipse described above and shown in Figure S4, and zero elsewhere. The remaining strain is then added to the strain from the previous (x, τ)-pair until either the probe reaches the opposite side of the sample or we run out of times for the pump. We repeat this process for different transmission delays and show the results of the cumulative strain in Figure S5. Because the path is a straight line, $|S|$ is constant and the same for all measurements.

Figure S5 shows the cumulative strain, computed using e_{yy}, for the P-wave probe and Figure S6 shows the cumulative strain, computed using e_{yz} for the S-wave probe. The first key point to note is that the cumulative strain is oscillatory, with the period of the pump, and with a shape that echoes the general shape of the pump, with some modifications caused by both boundary effects and from the integration. In the first panel of both figures, we test whether or not the waves interact primarily in the central region of the sample. This serves to test both whether or not inaccuracies in the model are strongly influencing the estimated accumulated strain and to test whether the central region of the strain field is more important to the interactions than the edge regions. For this test, we progressively remove more of the edges of the sample from the integration region. Specifically, before computing the integration we remove the contribution from the edges by setting $\epsilon_{AB}(x, Y_{max} - Y_{perc/2} < y < Y_{max}, z) = 0$ and $\epsilon_{AB}(x, Y_{min} < y < Y_{min} + Y_{perc}/2, z) = 0$, where Y_{max}/Y_{min} are the maximum/minimum y-value and Y_{perc}

is the percentage of the data set to zero and e_{AB} is the AB component of the strain tensor. From this plot, we see that the magnitude of the cumulative strain changes when we exclude parts of the sample, but the shape (as a function of time) does not. As a second test, we look at how the cumulative strain changes if we estimate it with different components of the modelled strain. This test is shown in (b) of Figure S5 and Figure S6. In this case, we see that the details of the shape change, but the strong component at the frequency of the pump remains whichever component of the strain we use. This gives us confidence that the cumulative strain is indeed an oscillatory function at the frequency of the pump. This helps to explain the signals that we observe; we see oscillations at the frequency of this cumulative strain with the sort of softening that is common in nonlinear experimental observations.

Table S1. Physical parameters for the numerical model.

Physical Parameters	
V_P	3.1 mm/μs
V_S	2.1 mm/μs
ρ	2.4 kg/m^3

xmax	ymax	zmax	dx=dy=dz	dt	f	nperiods	srad	sdir	fdir
radiation pattern 50 mm	155 mm	52 mm	0.75 mm	50 ns	200 kHz	1	5 mm	x	x
probe 50 mm	155 mm	52 mm	0.1 mm	10 ns	1 MHz	1	5 mm	x	x
PUMP 126 mm	155 mm	52 mm	1 mm	100 ns	100 kHz	4	12.5 mm	z	x

Table S2. Numerical parameters used in the experiments. nperiods is the number of periods

in the input source waveform (all use a sinusoid), sdir indicates the direction the source wave
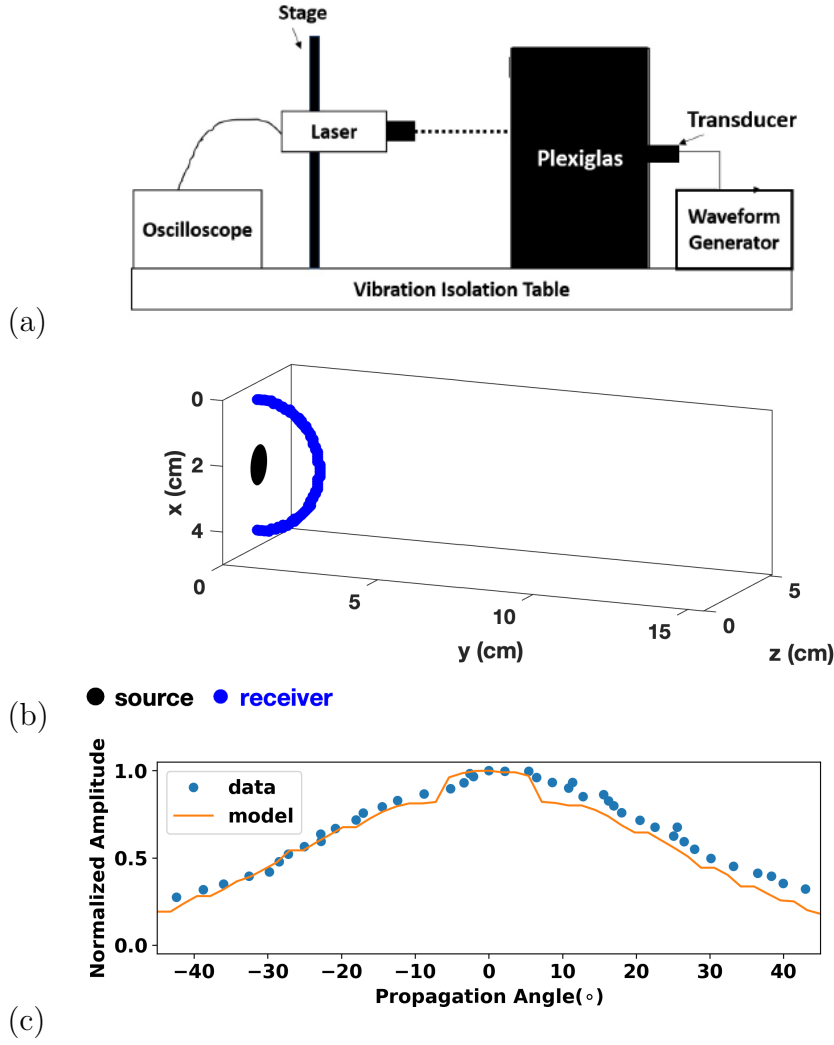
travels and fdir the direction of the applied force.

(a)

(b)

(c)

Figure S1. (a) Experimental configuration for measurement of the radiation pattern of the transducer. (b) Numerical experimental configuration for the measurement of the radiation pattern. (c) Comparison of the measured and modeled radiation patterns.
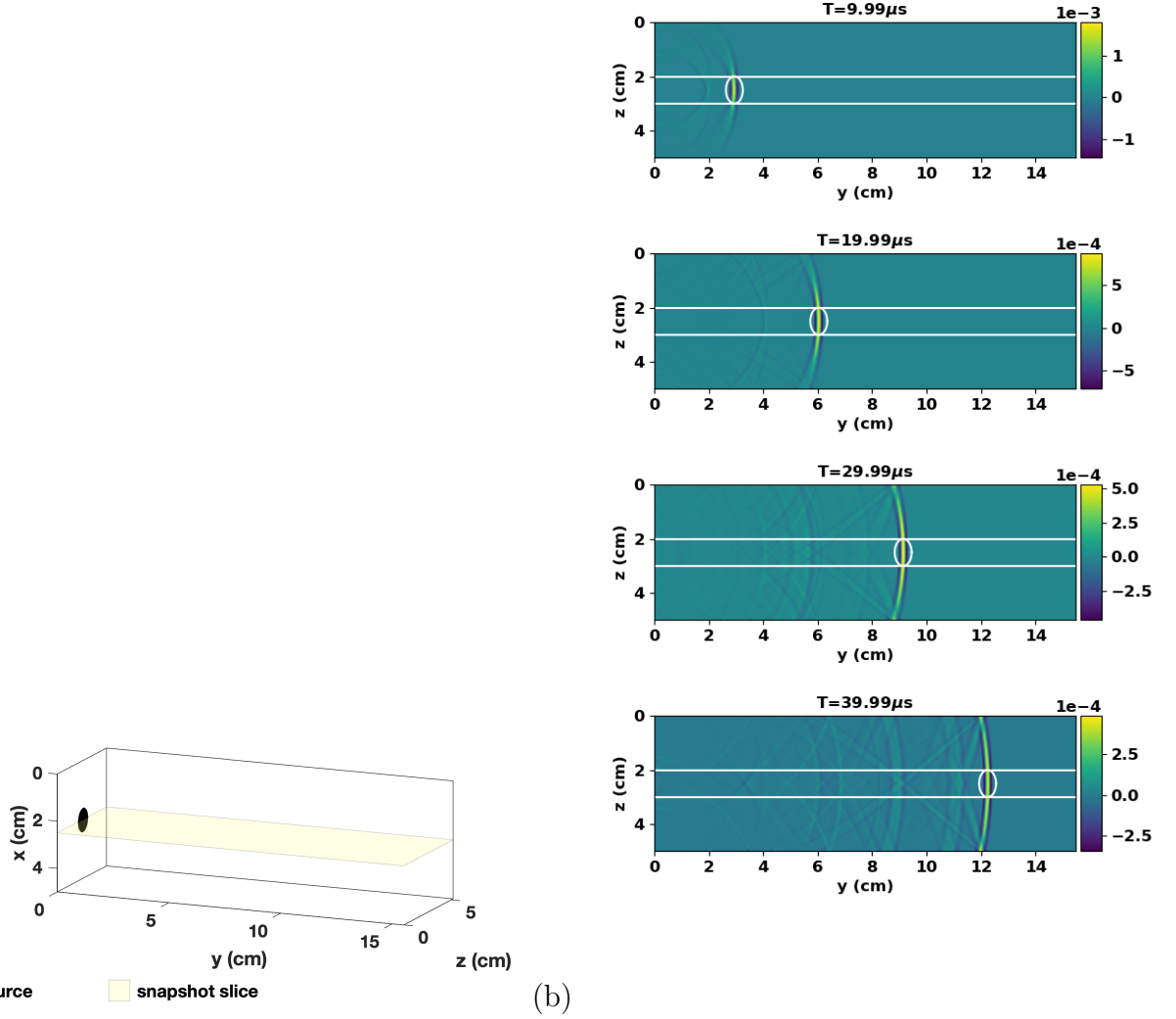
Figure S2. (a) Numerical Experimental Geometry for probe model. The yellow region highlights the location of the snapshots plotted below. (b) ϵ_{yy} for the probe signal at different times. The white lines show the boundaries of the transducer. The white ellipse shows the region included in the cumulative strain calculation. This shows that the probe signal is easily predicted.
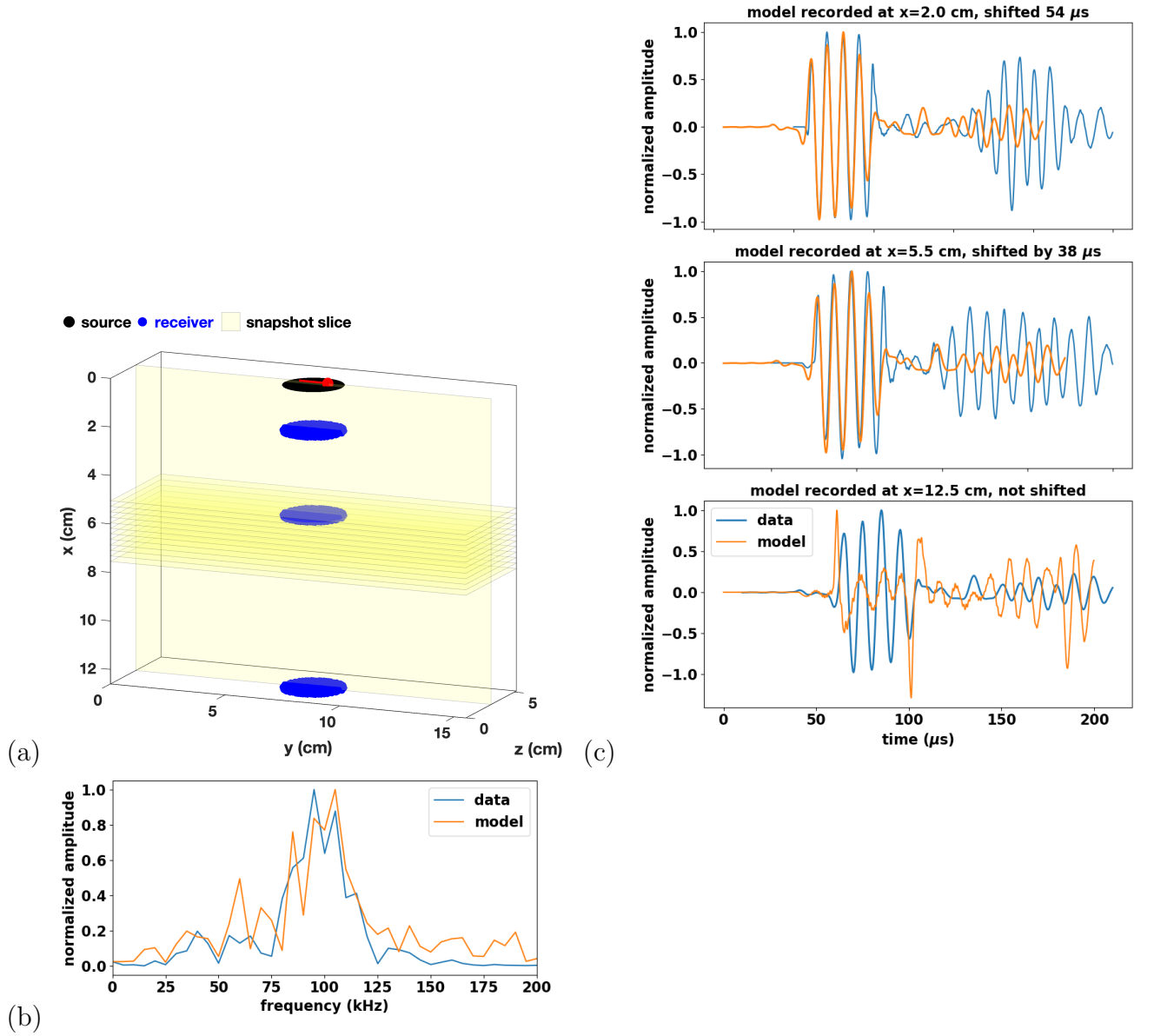
(a)

(b)

(c)

Figure S3. (a) Experimental setup for the PUMP model. The yellow regions show where snapshots are recorded; data from the vertical slice and the central horizontal slice are shown in Figure S4, and data from all of the horizontal slices are used in the computations shown in Figure S5. (b) Spectrum of the data (recorded at $(x, y, z) = (12.6, 7.5, 0.0)$ cm). (c) Comparison of the modeled and recorded signals at the top, middle, and bottom of the sample. The location of the receivers are shown as blue dots in the top panel. All data are normalized and we have shifted the experimental data to align with the first peak of the modeled data; the shifts are given in the individual plot titles.
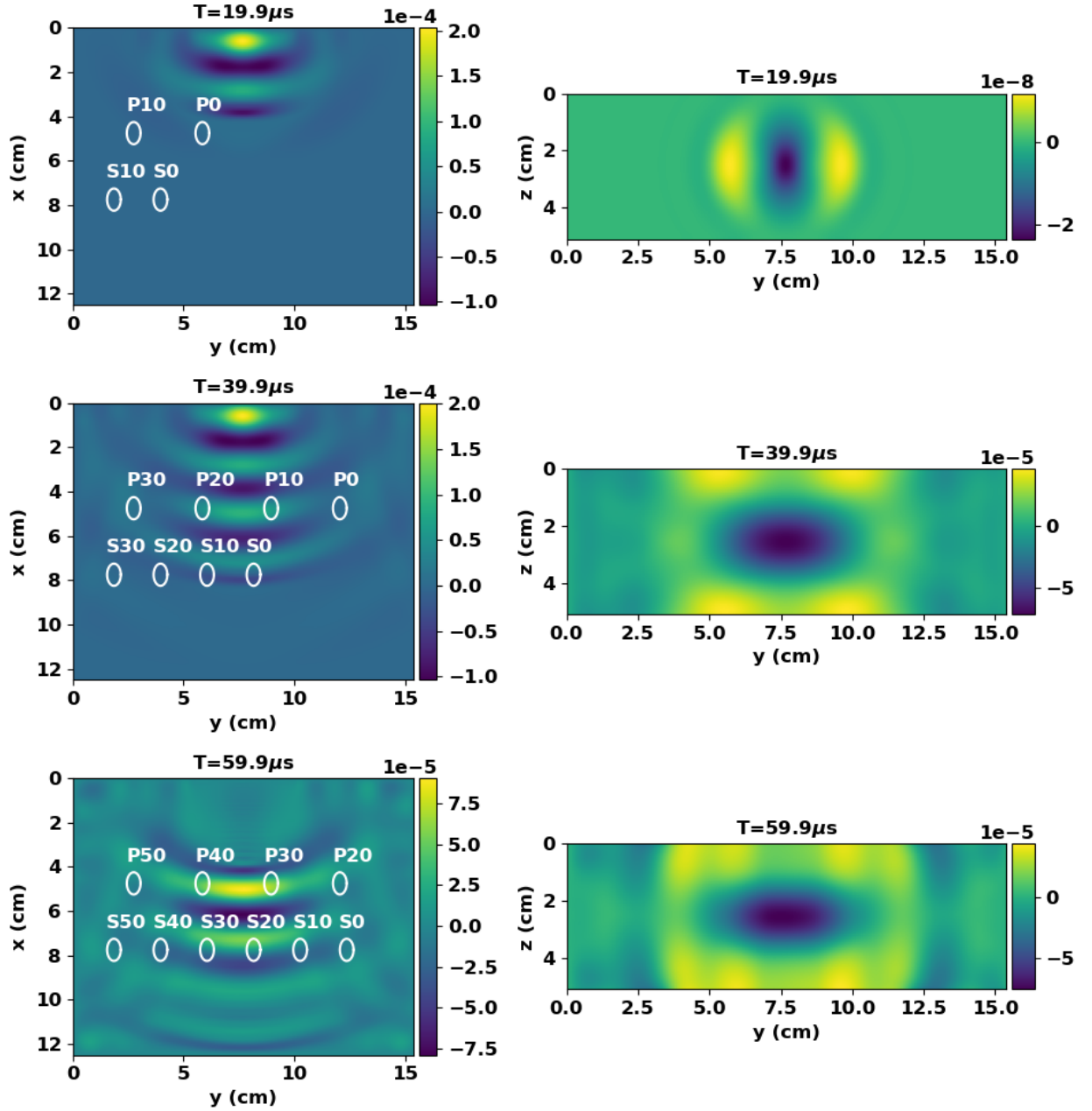
:

Figure S4. Snapshots of the PUMP wavefield (the e_{yx}-component as a function of time (plot title gives the time of the snapshot). The white ellipses outline the probe location for various delays (text above ellipses, in μs). The left column shows the vertical snapshot and the right column the central horizontal snapshots.
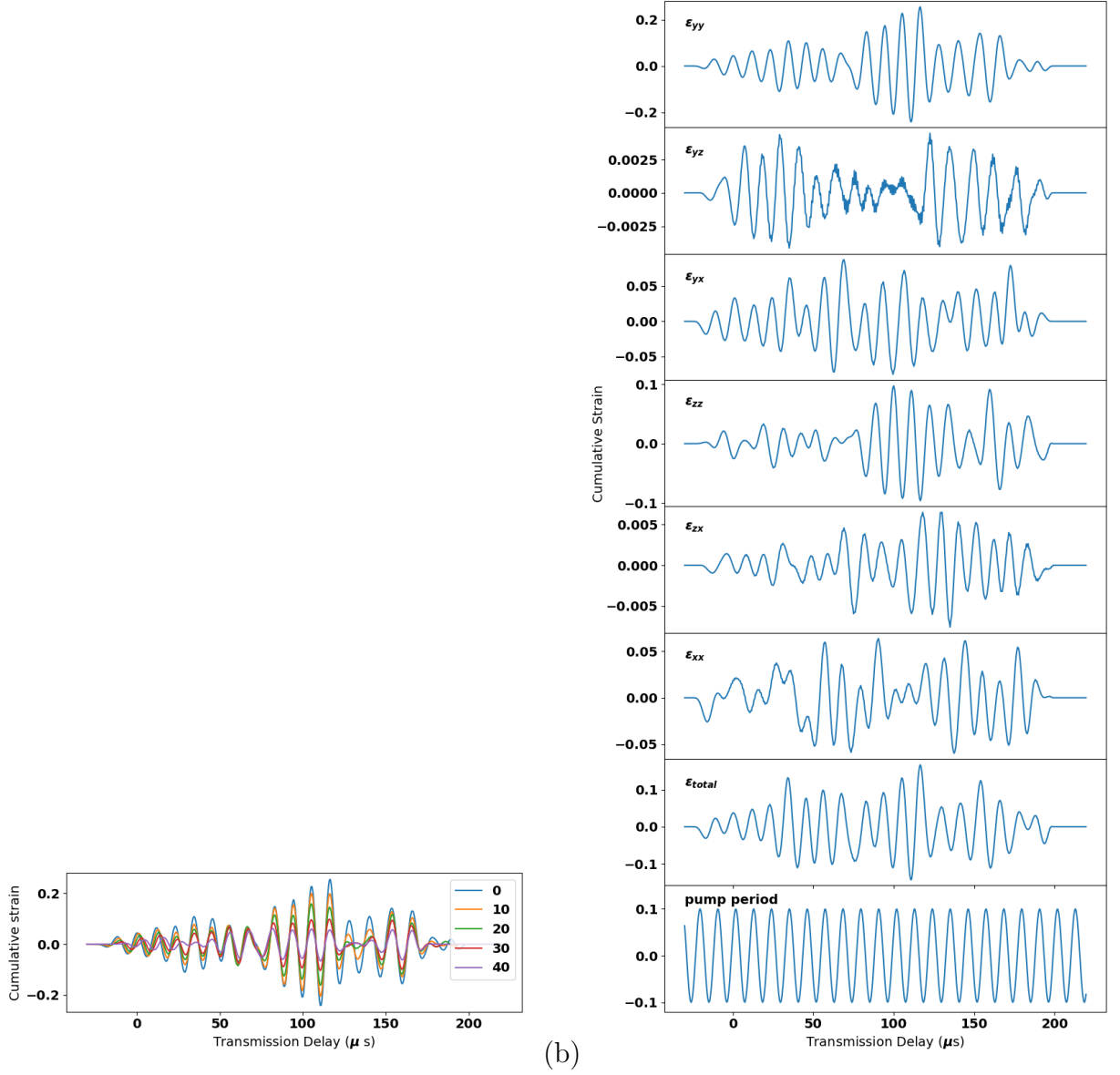
Figure S5. Cumulative strain for the P-probe. (a)Cumulative strain calculated with e_{yy}, as a function of the percentage Y_{perc}, of the model left out of the calculation (removed symmetrically from both sides); the legend number gives the value of Y_{perc} with units of %. (b) Cumulative strain computed using different input strain components. The bottom plot shows a sinusoid at the frequency of the pump with arbitrary phase. Note that each plot in (b) has its own y-axis values.
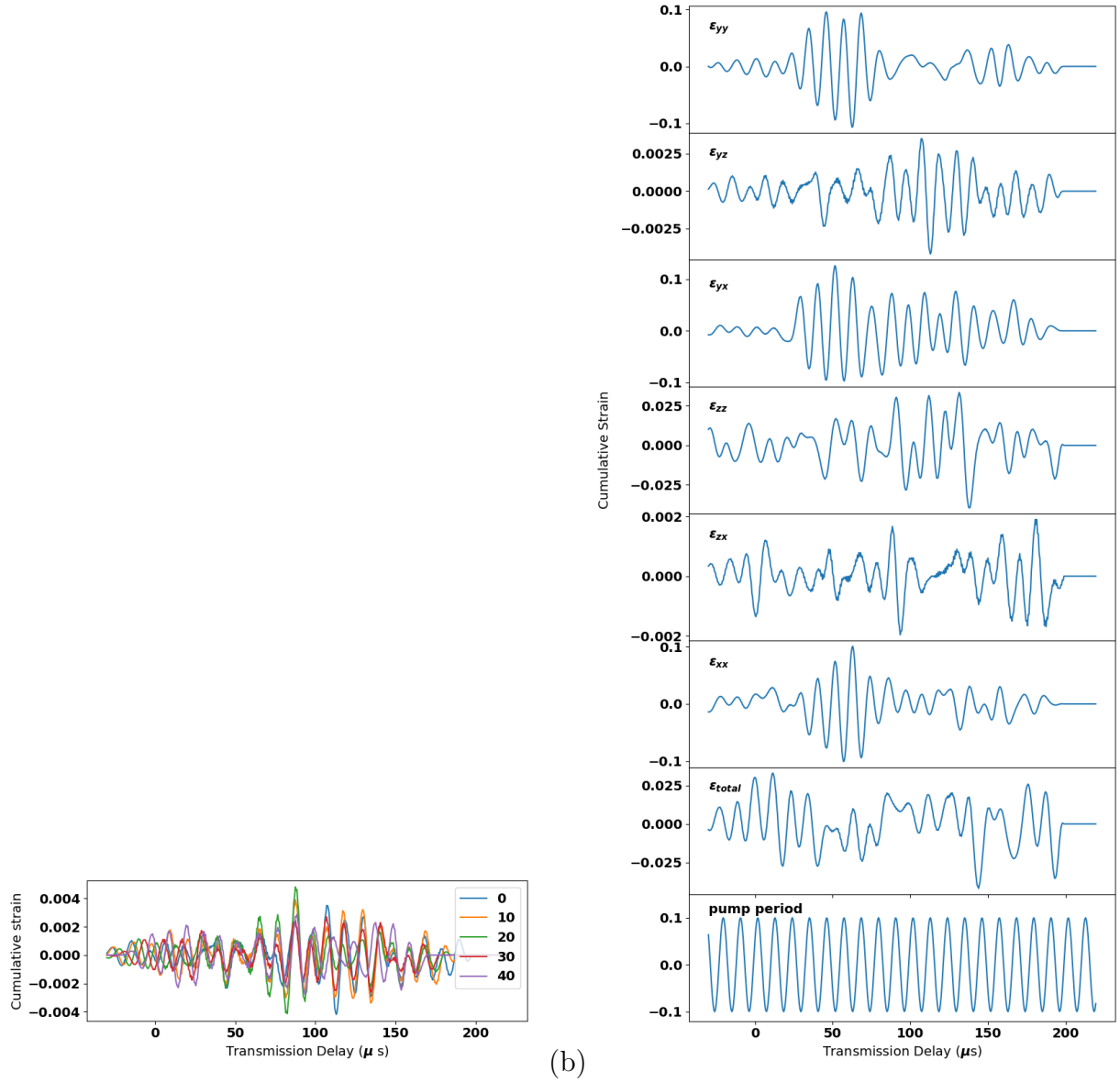
Figure S6. Cumulative strain for the S-probe. (a) Cumulative strain calculated with e_{xy} as a function of the percentage of the model left out of the calculation (removed symmetrically from both sides). (b) Cumulative strain computed using different input strains components. The bottom plot shows a sinusoid at the frequency of the pump with arbitrary phase. Note that each plot in (b) has its own y-axis values.